Journal of CO2 Utilization 99 (2025) 103163

Contents lists available at ScienceDirect

Journal of CO2 Utilization

journal homepage: www.elsevier.com/locate/jcou

Control of electrolyte intrusion in carbon-free silver gas diffusion electrodes for electrochemical CO_2 reduction

Inga Dorner [a], Jens Osiewacz [b], Philipp Röse [a], Barbara Ellendorff [b], Maximilian Röhe [a], Thomas Turek [b], Ulrike Krewer [a,*]

[a] Institute for Applied Materials – Electrochemical Technologies, Karlsruhe Institute of Technology, Adenauerring 20b, Karlsruhe 76131, Germany
[b] Clausthal University of Technology, Institute of Chemical and Electrochemical Process Engineering, Leibnizstraße 17, Clausthal-Zellerfeld 38678, Germany

ARTICLE INFO

Keywords:
CO_2 reduction
Gas diffusion electrode
Gas-liquid interface
Reaction-transport model
Faradaic efficiency
Concentration profiles

ABSTRACT

Achieving high conversion rates in electrochemical CO_2 reduction requires gas diffusion electrodes to ensure sufficient CO_2 availability at the electrode surface. Carbon-free Ag electrodes offer superior stability compared to carbon-based ones but are challenged by complex electrolyte intrusion and distribution. This study combines experimental variations in electrode design and operating parameters with modeling to identify key factors for high Faradaic efficiency towards CO and high current densities. Results emphasize the importance of an optimal gas/liquid interface. Increasing gas-side overpressure from 60 to 100 mbar doubled the Faradaic efficiency for CO from 20 % to 42 % at 200 mA cm^{-2} due to higher local CO_2 concentrations in electrolyte-flooded regions. Thin electrodes of 200 μm outperformed thicker ones up to 390 μm, achieving higher efficiencies by enhancing CO_2 and electrolyte transport, which lowered local pH levels. Optimizing PTFE content further improved performance; reducing PTFE from 2 to 1 wt% increased Faradaic efficiency by 20 % at 200 mA cm^{-2} by balancing hydrophobicity and active surface exposure. These insights into the relationship between electrode properties, operating conditions, and gas-liquid distribution advance the design of gas diffusion electrodes for competitive CO_2 reduction applications.

1. Introduction

Electrochemical CO_2 reduction (CO_2R) is a technology that promises to enable a sustainable life cycle of CO_2 and, as a negative CO_2 emission technology, it contributes to mitigating the ongoing rise in atmospheric carbon dioxide emissions [1].

CO_2 is electrochemically reduced to carbon monoxide on catalysts such as silver (Eq. (1)) [2]. The process achieves high current densities, high Faradaic efficiency at moderate current densities, and durability, positioning it as a promising CO_2R technology. However, practical applications remain limited [3,4]. The primary challenge lies in the mass transport limitation of CO_2 attributed to the low solubility of CO_2 in the aqueous electrolyte. This limitation leads to CO_2 depletion at higher current densities and favors the competing hydrogen evolution reaction (HER) (Eq. (2)) [5–7].

$$CO_2 + 2e^- + H_2O \rightarrow CO + 2OH^- \quad (1)$$

$$2H_2O + 2e^- \rightarrow H_2 + 2OH^- \quad (2)$$

Additionally, it has been demonstrated that an increase in local pH due to the formation of hydroxide ions favors the chemical consumption of CO_2 by the carbonate reactions, converting it to bicarbonate and carbonate (Eqs. (3) and (4)) [8,9].

$$CO_2 + OH^- \rightleftarrows HCO_3^- \quad (3)$$

$$HCO_3^- + OH^- \rightleftarrows CO_3^{2-} + H_2O \quad (4)$$

This decreases the local CO_2 concentration, further exacerbates the challenge of limited CO_2 availability and, thus, Faradaic efficiency [7,10]. A characteristic that sets electrochemical against chemical consumption of CO_2 is the so-called carbon efficiency (CE).

$$CE = \frac{\dot{n}_{CO_2,elchem}}{\dot{n}_{CO_2,elchem} + \dot{n}_{CO_2,chem}} \quad (5)$$

To improve CO_2 availability and attain industrially relevant current densities $\geq$ 200 mA cm^{-2}, gas diffusion electrodes (GDEs) are employed [11]. In GDEs, the CO_2 gas is supplied from one side of the electrode, and

* Corresponding author.
E-mail address: ulrike.krewer@kit.edu (U. Krewer).

https://doi.org/10.1016/j.jcou.2025.103163
Received 11 February 2025; Received in revised form 1 June 2025; Accepted 19 June 2025
Available online 24 June 2025

electrolyte is supplied from the other side. Both phases converge at distinct locations within the gas diffusion electrode, where they form the gas/electrolyte interface. This ensures a high availability of CO_2 over a wide catalyst area in the GDE and mitigates the CO_2 transport limitation in the electrolyte-flooded part of the GDE caused by the low CO_2 solubility in the electrolyte. However, the quantitative description, adjustment, and prediction of GDE performance become considerably more complex compared to a flat or flooded porous electrode due to the high sensitivity to the electrolyte intrusion state in the GDE which also depends on the porous electrode structure [12]. This motivates intensive research to understand and design optimal GDE compositions and structures [13].

Commonly studied GDEs in CO_2R consist of a carbon-based gas diffusion layer (GDL) coated with an optional hydrophobic microporous layer (MPL) and an overlying porous catalyst layer that is in contact with the electrolyte [14,15]. The catalyst layer provides the electrochemically active surface area (ECSA), which is essential for the reduction reaction. The MPL, typically made of carbon black and polytetrafluoroethylene (PTFE) particles, minimizes electrical contact resistance between GDL and catalyst layer and creates a hydrophobic barrier to prevent complete electrode flooding by the electrolyte. Several studies investigated the impact of electrode structure on electrolyte distribution, flooding behavior, and performance.

A recent study found that thicker MPLs reduced Faradaic efficiency for CO (FE_{CO}) at low current densities due to increased CO_2 transport resistance, but that they improve performance at higher current densities by resisting flooding and salt precipitation [16]. Additionally, cracks in the MPL were shown to mitigate the decline in the FE_{CO} at higher current density by enhancing access to fresh electrolyte solution, allowing a deeper electrolyte penetration into the microporous layer of the electrode structure. This increased the overall capacity to store salt precipitates and decreased the blockage of ECSA [17].

The hydrophobicity of the electrode is adjusted by adding hydrophobic polymers like PTFE. Yet, PTFE may cover the catalyst surface and is thus expected to reduce the ECSA [18]. However, opposing trends, such as an increase of ECSA with higher PTFE amounts, have also been observed [19]. Both observations suggest a complex interplay among electrolyte intrusion, catalyst surface area, surface roughness, PTFE coverage, and PTFE degradation, as all of them impact the effective electrochemically active surface area. This interaction is not yet fully understood, hampering knowledge-driven design of electrodes and operating conditions for a high and long-term stable performance of CO_2R.

Heßelmann et al. [20] proposed in a simulative study with a one-dimensional steady-state model that increasing the porosity of a 3 μm thick catalyst layer and reducing the catalyst loading results in a decrease in FE_{CO} [20]. This implies that the decrease in surface area outweighs the benefits gained from improved mass transport in their case.

All studies mentioned before [16–20] provided insights into electrolyte intrusion-related processes that influence Faradaic efficiency and current density at a given potential. These studies are confined to carbon-based electrodes, which are the electrodes most frequently used in CO_2 reduction research so far. However, these electrodes face significant stability issues for CO_2R applications due to susceptibility to flooding [21]. Moreover, studies were carried out with many different GDLs, which differ in terms of the carbon structure, thickness, porosity, etc. This makes a systematic comparison difficult [14].

As an alternative, carbon-free electrodes have shown promising performance [22]. Besides using GDLs based on metal [23,24], PTFE [25], or membranes [26], carbon-free silver GDEs without a separate GDL, which are known from commercial use for oxygen reduction reaction in chlor-alkali electrolysis [27], can be used for CO_2 reduction. The latter electrodes consist of a porous structure made from a mixture of Ag catalyst particles and PTFE binder coated on a metal mesh, which serves as a current collector and mechanical support. PTFE particles, typically ranging from 1 to 10 wt% serve to adjust the wanted hydrophobicity. The catalyst loading ranges between 140 and 250 mg cm^{-2} for electrode thicknesses of around 200–400 μm. These carbon-free Ag GDEs provide a high ECSA and exhibit a long lifetime in ORR [28] and in CO_2R [4,29,30].

In addition to their promising long-term stability, these electrodes were selected for this study due to the extensive prior characterization and prior gained understanding of the processes occurring within them. In the context of ORR, transport processes, electrolyte distribution, and reaction interaction have been extensively investigated for these electrodes, both experimentally and by simulations. A critical challenge is the slow water transport in and close to these relatively thick electrodes resulting in elevated ion concentrations within the reaction zone of the electrode [31]. Utilizing electrochemical impedance spectroscopy in combination with kinetic modelling, we were able to detect a strongly heterogeneous flooding behavior, discernible as flattened semicircles in the Nyquist plot [32]. This behavior signifies the absence of a straight electrolyte/gas front within the electrode, distinguishing it significantly from the state in carbon-based electrodes. Instead, it displays a pore-selective, capillary force-driven intrusion of the electrolyte, which is promising for high gas/liquid interfaces. Such strong inhomogeneity is also expected to prevail for CO_2R; it remains unanswered so far, how the inhomogeneity in electrolyte distribution affects CO_2R.

The characteristics of alkaline electrolyte intrusion into carbon-free GDEs were visualized experimentally by Paulisch et al. [33] for ORR, and by Hoffmann et al. [34] for CO_2R using operando laboratory x-ray imaging. In the latter study, it was found that a GDE with 97 wt% Ag content (3 wt% PTFE) was more beneficial for CO_2R than with 92 wt% Ag. This was attributed to a larger triple-phase boundary during operation, resulting in a better CO_2 availability [34].

Osiewacz et al. [35] developed a comprehensive model for analyzing these electrodes in CO_2R. They revealed that electrodes with 97 wt% Ag primarily suffer from slow CO_2 mass transport and a strong carbonation reaction, resulting in a low carbon efficiency and a low Faradaic efficiency at high current densities $\geq$ 300 mA cm^{-2}. They also predicted with their model that thinner electrodes may become more selective for CO production [35].

When comparing carbon-free with carbon-based electrodes, Baumgartner et al. [36] deemed the carbon-free electrode unsuitable for CO_2 reduction due to its significantly higher susceptibility to flooding [36]. However, a systematic investigation of the influence of electrode and operating parameters on carbon-free GDEs is still pending. The impact of electrolyte intrusion and distribution on electrode performance remains an open question so far. Yet, this aspect is crucial for improving these electrodes to make them suitable for CO_2R.

In the study presented here, we reveal how operating and design parameters impact performance by changing the intrusion of the electrolyte into Ag GDEs. Operating parameters and electrode composition are systematically varied, and their effects are studied. The parameters include the differential pressure between gas and electrolyte side, electrode thickness, and PTFE content. These parameters were selected based on their reported relevance to process performance in prior studies [37–39] and their practical adaptability. In these studies, their primary influence is attributed to effects on the CO_2 availability in the electrode, transport distance for ions, and electrolyte distribution within the electrode. To gain a comprehensive understanding of the relation between these parameters, intrusion state, and performance, we utilize a physicochemical model that is parameterized and validated by experiments (Fig. 1). The porous electrode is partly flooded, such that one region contains gas while another is filled with liquid electrolyte. The flooded region, referred to as the flooded agglomerate, is characterized by its thickness d_{fa}. It defines a two-phase boundary between the electrolyte and the catalyst surface, thereby determining the ECSA where electrochemical reactions take place. To reduce model complexity while retaining the essential physics, the following assumptions were applied:

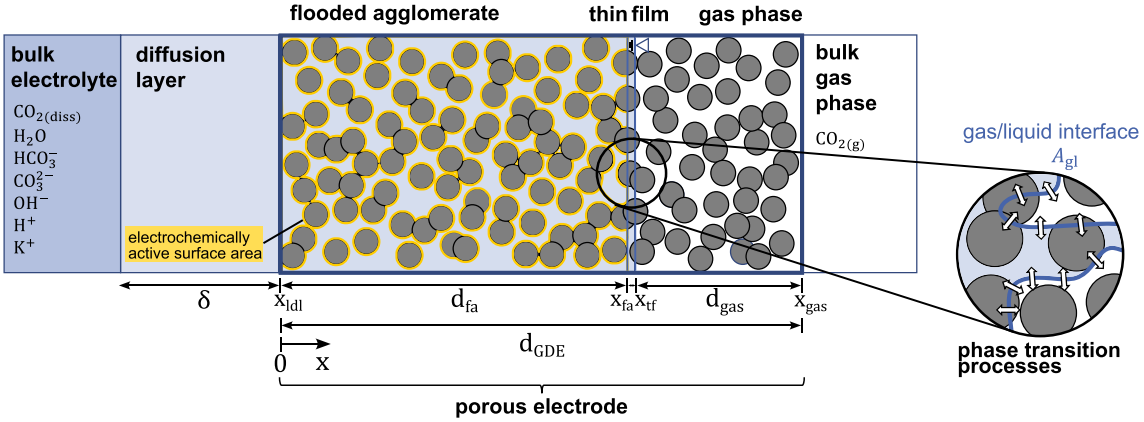

Fig. 1. Scheme of gas diffusion electrode model for CO_2 reduction.

- Migration and diffusion, and Stefan flow in the gas phase are considered as the main transport processes; capillary forces or gravity effects are neglected.
- Electrochemical reactions are assumed to take place in the flooded agglomerate, and carbonation reactions in the flooded agglomerate and the liquid diffusion layer.
- The model is one-dimensional; considering concentration and state changes only perpendicular to the electrode surface, i.e., transport occurs only through-plane.
- Temperature and electrode properties are uniform and constant.
- The intrusion state and gas–liquid interface position are assumed constant over time and independent of the applied current density.
- Precipitation of salt is neglected.

The model provides detailed insights into current-dependent profiles of local species concentrations, pH gradients, Faradaic efficiencies, and their impact on electrode potential. This investigation sheds light mechanistically and quantitatively on limiting processes within these electrodes, offering valuable essential for optimization of electrode design and operation. To the best of our knowledge, such a rigorous analysis of electrolyte intrusion and distribution within such GDEs and its model-assisted interpretation is novel and has not yet been addressed in the literature.

2. Results and Discussion

The following analysis of the impact of flooding behavior on electrode performance employs a combined approach of experimental and simulation methods. For the experiments, we varied the differential pressure between the electrolyte and gas side of the GDE, the electrode thickness, and the mass content of PTFE in the GDE. The GDEs were operated in a flow cell setup in a three-electrode configuration with aqueous 1 M $KHCO_3$ as an electrolyte (*cf.* Section 4.2. and Table 2). Performance assessment was based on polarization curves and FE_{CO}, recorded at current densities between 10 and 200 mA cm^{-2}, a range in which stable operation of the GDEs can be ensured. A 1D physicochemical model for CO_2R in Ag GDEs (*cf.* Section 5 and Fig. 1) was used to identify changes in electrolyte intrusion for the different electrodes and operating conditions and their impact on local concentration and current distribution as well as on electrode performance. Transport and reaction parameters of the model were parametrized based on experimental polarization curves and Faradaic efficiency-current density relationships obtained for the individual parameter sets (*cf.* Section 5.2.).

2.1. Current and concentration distribution along the GDE

First, we reveal the effects of concentration profiles and current distribution along the electrode thickness on the electrode potential and Faradaic efficiency for different current densities. The analysis was conducted at the example of a Ag GDE with a thickness of 392 µm (equivalent to 80 layers of spray coating, *cf.* Section 4.1), a PTFE mass fraction of 3 wt%, and an overpressure of 60 mbar from the gas side to the electrolyte side. The catalyst loading was 166 mg_{Ag} cm^{-2}. The experimental polarization curve (Fig. 2A) reveals a monotonic logarithmic decrease in potential with increasing current density, with no apparent limiting current observed within the investigated range. FE_{CO} reaches a peak of 70 % at a low current density of 20 mA cm^{-2} and decreases subsequently monotonically as current density increases (Fig. 2B). The simulation accurately reproduces both, the current-potential and FE_{CO}-current density trends.

The peak in FE_{CO} can be attributed to the kinetic interplay between CO_2R and HER: At high potentials close to open circuit potential, i.e., at low current densities, HER significantly competes with CO_2R due to its more positive onset potential, reducing FE_{CO} (Figure S1). As current density increases, CO_2R becomes the dominant process, resulting in an upsurge in FE_{CO}. A similar observation is made in kinetic studies conducted on planar silver electrodes [40,41].

Already, at a current density of 25 mA cm^{-2}, where FE_{CO} reaches its maximum in the simulation, a nonuniform current (Fig. 3A) and concentration distribution (Fig. 3C, dashed lines) are present along the flooded agglomerate. Close to the liquid diffusion layer ($x = 0$), there is a slight increase in Faradaic current for CO due to an elevated CO_2 concentration at this boundary provided by the equilibrium concentration of CO_2 in 1 M $KHCO_3$ electrolyte. In proximity to the gas/liquid interface ($x = d_{fa}$), the highest CO_2 concentration is present, resulting in the highest FE_{CO} at this interface compared to the rest of the electrode. The high CO_2 concentration also lowers the pH in this area. Thus, the lowest local currents and Faradaic efficiency are found in the middle of the electrode.

The situation inside the flooded part of the electrode changes dramatically for higher current densities: FE_{CO} decreases for higher current densities and is almost zero over a large part of the flooded agglomerate at a current density of 200 mA cm^{-2} (Fig. 3B). Thus, a significant part of the flooded GDE is not active for CO_2R. This decline can be attributed to the increasing CO_2 depletion within the electrode, evident in low local CO_2 concentrations in most of the electrode (Fig. 3C). At this current density, almost all incoming CO_2 is directly reduced adjacent to the gas/liquid interface, and a huge part of the wetted catalyst surface lacks CO_2. This phenomenon is mainly induced by a thick electrolyte layer between the gas and the catalyst surface within the electrolyte-flooded electrode. A high value leads to long diffusion distances for dissolved CO_2 and strong transport limitations in most parts of the electrode, which in turn promotes HER.

Additionally, the local pH within the electrode increases from 10 to approximately 13 with increasing current density (Fig. 3C). At 200 mA cm^{-2}, the pH profile displays a peak located in the flooded

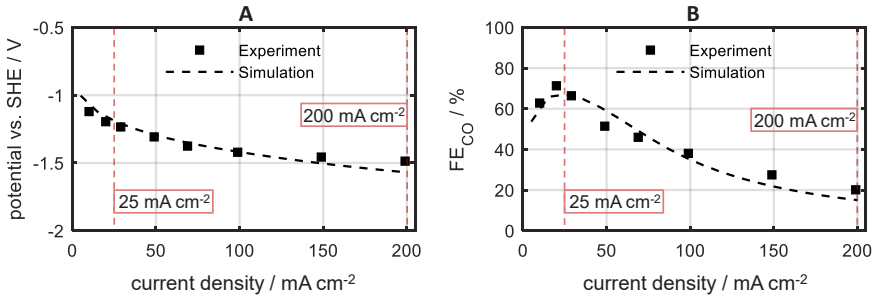

Fig. 2. Experimental and simulated (A) polarization curves and (B) Faradaic efficiency of carbon monoxide (FE_{CO}) for a GDE with 392 μm electrode thickness, 3 wt% PTFE, and a differential pressure of 60 mbar between gas and electrolyte side. Two current densities are highlighted. Measurements were done in a flow cell with 1 M $KHCO_3$, and potentials are iR-corrected.

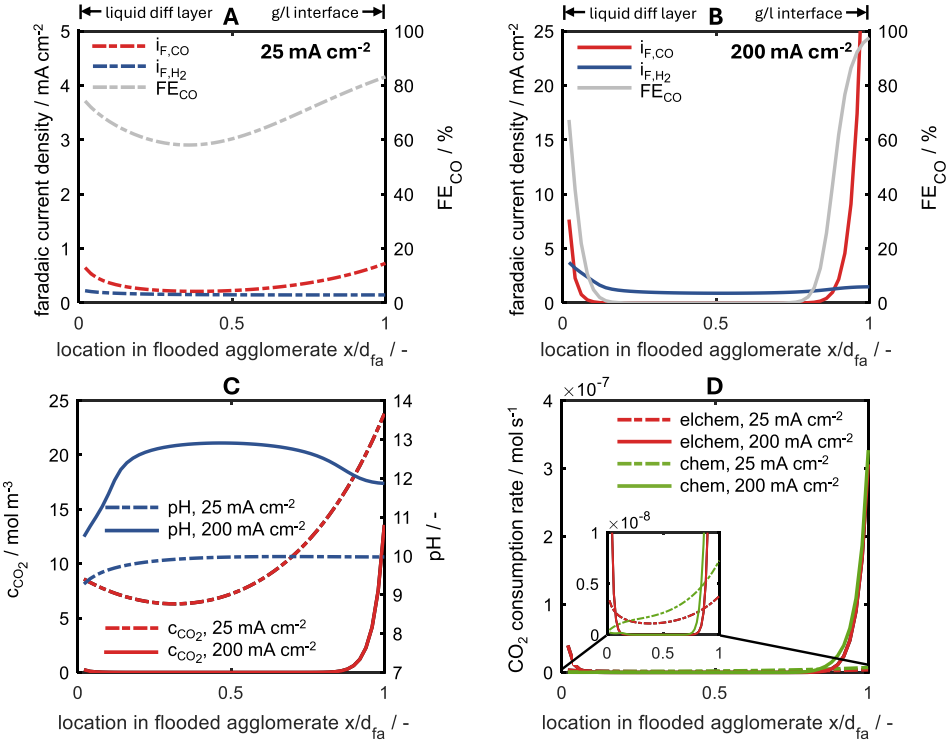

Fig. 3. Simulated local profiles of Faradaic current densities for CO and H_2 production, respectively, and FE_{CO} along the flooded agglomerate (fa; boundary to liquid diffusion layer at $x = 0$, gas at $x = 1$) for operation at (A) 25 mA cm^{-2} and (B) 200 mA cm^{-2}. (C) Local CO_2 concentration and pH along the flooded agglomerate for 25 mA cm^{-2} and 200 mA cm^{-2}. (D) Chemical and electrochemical CO_2 consumption rate and carbon efficiency CE along flooded agglomerate for 25 mA cm^{-2} and 200 mA cm^{-2}. GDE and operating parameters are: 350 μm thickness, 3 wt% PTFE, and 60 mbar differential pressure in a flow cell with 1 M $KHCO_3$.

agglomerate's center. Close to the liquid diffusion layer and the electrolyte bulk, OH^- concentration diminishes due to OH^- diffusion out of the flooded electrode and fresh electrolyte supply. Fresh electrolyte provides a high bicarbonate concentration, which promotes its reaction with OH^- to carbonate. Near the gas/liquid interface, the low pH results from a high carbonation reaction, facilitated by ample CO_2 availability. Both effects can be clearly seen in the local distribution of the chemical consumption rate of CO_2 (Fig. 3D). At the gas/liquid interface ($x/d_{fa} = 1$), electrochemical CO_2 consumption increases similarly as the chemical CO_2 consumption due to good CO_2 availability and a pronounced buffer effect by the CO_2-to-bicarbonate reaction. In contrast, at the electrolyte side ($x/d_{fa} = 0$), although CO_2R increases due to higher CO_2 concentrations, chemical CO_2 consumption does not increase. The increasing pH is buffered mostly by the bicarbonate-to-carbonate reaction due to the high supply of fresh bicarbonate electrolyte.

These insights vividly illustrate that the local condition profile in the electrode determines overall electrode performance. Not only does the CO_2 supply from the gas phase affect it, but also the pH determines the distribution of CO_2R and HER. As the FE_{CO} is so sensitive to local pH and thus to local transport conditions and CO_2 availability, this motivates to improve FE_{CO} by manipulating the transport and local conditions. It is thus reasonable to expect that by optimizing operating and design parameters, a low Faradaic efficiency can be significantly increased. Hence, in Section 2.2, we will show how the operating and design variation impact electrolyte intrusion, and how this, in turn, impacts local conditions and performance. This allows knowledge-driven design, i.e., to reveal ways in which the GDE properties and operating conditions can be tailored to improve the CO_2R performance and Faradaic efficiency.

2.2. Electrolyte intrusion behavior of the GDE

As revealed in the last section, electrolyte intrusion behavior has a crucial impact on the local state and thus on the electrode performance.

To gain insight into this aspect, we conducted a comprehensive study on selected electrode and operating parameters. The varied parameters include electrode thickness, PTFE mass fraction in the electrode, and differential pressure between liquid and gas sides. Experimental polarization curves and FE-current density curves were successfully reproduced through simulations. From the simulation, we extracted parameter values for the volumetric electrochemically active surface area ($ECSA_v$ ($m^2\ m^{-3}$)) and the apparent thickness L of the electrolyte layer between the gas and the catalyst [42]. $ECSA_v$ characterized the catalytic activity provided by the wetted parts of the electrode. L depends on the electrolyte arrangement in the electrode, *i.e.*, electrolyte intrusion depth d_{fa} and size of gas/liquid interface S_{gl}, and defines at the same time the maximum transport distance of the dissolved CO_2 to the catalyst surface (Fig. 4, more information in Section 2 of the Supporting Information). In the following, $ECSA_v$ and L are discussed, as they proved to be the most meaningful parameters with regard to electrode behavior. These parameters were calculated using the following equations:

$$ECSA_v = d_{fa} \cdot a_{cat} \cdot d_{GDE}^{-1} \tag{6}$$

$$L = d_{fa} \cdot S_{gl}^{-1}. \tag{7}$$

Here, d_{GDE} represents the thickness of the electrode, d_{fa} is the thickness of the flooded agglomerate, a_{cat} is the specific surface area of the Ag catalyst per electrode volume, and S_{gl} denotes the specific surface area of the gas/liquid interface per geometrical electrode area (see Eq. (16)). d_{fa}, a_{cat}, and S_{gl} were identified by parameter optimization. The specific surface area of the Ag catalyst a_{cat} was identified in a narrow range to a value of $6.25 \times 10^5\ m^2\ m^{-3}$ for a PTFE content of 3 wt%. A similar value was determined by Neumann et al. with tomographic reconstruction of a porous electrode structure with the same PTFE content (for detailed information see Section 5.1.) [43].

2.3. Influence of electrode thickness

To investigate the impact of electrode thickness, we adjusted the GDE thickness by varying the number of layers between 50 and 110 layers during the spray coating process of electrode preparation. The resulting electrode thickness was measured after sintering. The examined electrodes had thicknesses of 200, 275, and 390 μm. The differential pressure and PTFE content were kept constant at 100 mbar and 1 wt % PTFE, respectively. The corresponding current density-potential and FE_{CO}-current density curves are presented in Fig. 5A and B.

At low current densities, the thicker electrodes exhibit slightly more positive electrode potentials, indicating better performance. However, at higher current densities, potentials are nearly identical for all thicknesses. FE_{CO} values are quite similar but slightly higher for thicker electrodes at low current densities $< 50\ mA\ cm^{-2}$ and lower at higher current densities. Consequently, thinner electrodes seem to be slightly more selective for CO_2 reduction compared to HER in the technically relevant current density regime $\geq 200\ mA\ cm^{-2}$. However, the performance is relatively robust against variations in electrode thickness under the given operating conditions. It can be further concluded that there is no simple relation between a change in thickness and improvement in the total current range regarding both performance measures, *i.e.,* electrode potential and FE_{CO}. This again suggests a complex interplay of parameters and processes with changes in limiting processes, which we analyzed in the following.

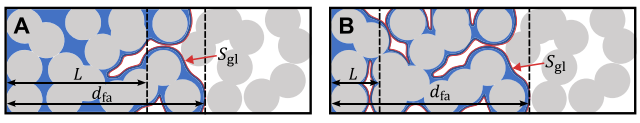

Fig. 4. Illustration of possible electrolyte arrangements in porous GDE with (A) low gas/liquid interface S_{gl} resulting in a large, apparent thickness L of electrolyte layer between the gas and the catalyst surface and with (B) high S_{gl} resulting in low values of L.

The model reproduced the trend, both for the polarization curve and the FE_{CO}. The corresponding simulation results suggest that if we look at thick electrodes, smaller potential losses at low currents $< 50\ mA\ cm^{-2}$ can be attributed to the larger area-specific electrochemically active surface area $ECSA_a$, provided by the larger amount of wetted catalyst material compared to thinner electrodes (Fig. 5C). The slightly increased FE_{CO} for thinner electrodes at high current densities can be explained as follows: Firstly, the CO_2 concentration in the electrode is lower for larger electrode thickness (Fig. 5D) as the molecules are spread over a wider volume. This results in a decrease of FE_{CO} in the whole electrode for thicker electrodes (Fig. 5E). Secondly, the local pH is shifted to slightly lower values for thinner electrodes, which can be explained by the smaller distance of transport for dissolved species to and from the electrolyte bulk. This distance depends on electrolyte intrusion, characterized by the length of the flooded agglomerate d_{fa}. Thinner electrodes experience significantly less flooding length, leading to enhanced electrolyte transport, *i.e.*, a better removal of hydroxide ions and an improved supply of bicarbonate and carbonate species. This, in turn, results in a stronger buffering effect by the bicarbonate-to-carbonate reaction and in a lower pH. The shift to bicarbonate-to-carbonate reaction is reflected in a higher carbon efficiency within the flooded agglomerate compared to thicker electrodes ((Fig. 5 F) and Eq. (5)). The CE is significantly higher for thinner electrodes with a mean value of 52 % compared to 43 % for the thick electrode at $200\ mA\ cm^{-2}$.

The effect of slow electrolyte transport in the porous Ag electrode structure was also observed in cathodes of oxygen reduction reaction [31]. Our observation of improved performance with better transport of dissolved electrolyte species aligns with Kong et al. [17], who reported enhanced electrode performance when fresh electrolyte was introduced through cracks [17].

Consequently, the performance of CO_2 consuming GDEs is not only limited by CO_2 transport itself, but also by slow electrolyte transport in and out of the electrode, which diminishes FE_{CO} and carbon efficiency for thick electrodes. This explains the downside of carbon-free silver electrodes which typically have relatively high electrode thicknesses, and thus suffer more from slow CO_2 and electrolyte transport.

2.4. Influence of differential pressure

One of the most critical operating parameters for gas diffusion electrodes is the differential pressure between the gas and the electrolyte side. Maintaining an overpressure from the gas side is essential to prevent complete flooding of the electrode pores with liquid electrolyte [44, 45]. The differential pressure has a substantial influence on the intrusion of electrolyte into the electrode. In this section, we delve into the detailed effects of differential pressure on local reaction conditions and current density distribution. We aim to draw conclusions about electrolyte distribution and the potential for performance enhancement through optimized operating conditions.

The overpressure from the gas side was varied between 20 and 100 mbar while keeping the electrode properties constant (3 wt% PTFE and 80 layers of spray coating). Due to the electrode preparation process, there are slight deviations in the electrode thickness d_{GDE} in this series of measurements (Table 1). Yet, they are shown to have a negligible impact compared to the effect of pressure (Figure S2 and Figure S3). For this reason, larger differences in performance can be attributed to the variation of the operating parameter, *i.e.,* the differential pressure.

The experimental polarization curve in Fig. 6A reveals a marginal improvement in potential with increasing differential pressure at all applied current densities. Using the model, the improvement can be attributed to an increase in $ECSA$ (Fig. 6C), which is caused mostly by an increase in flooded agglomerate thickness: Changing the differential pressure from 20 to 100 mbar results in a change in the flooded

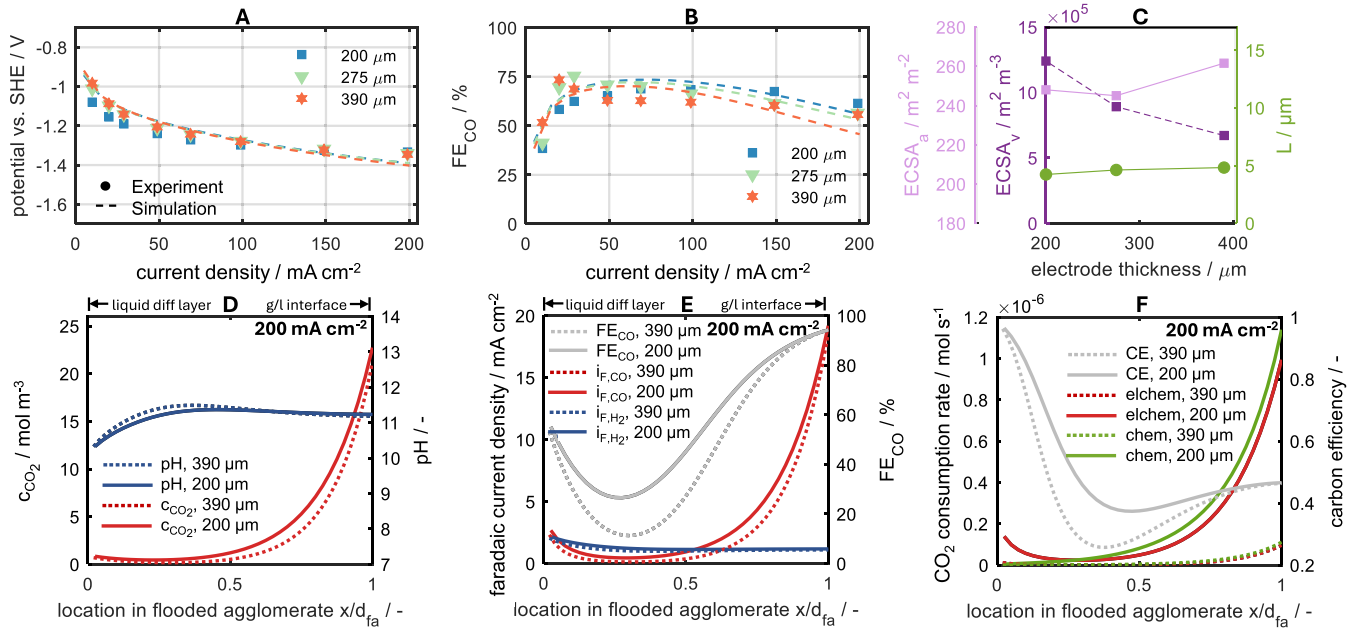

Fig. 5. Impact of electrode thickness on GDE performance and state: Experimental and simulated (A) polarization curves and (B) FE_{CO} (differential pressure: 100 mbar, PTFE content: 1 wt%). (C) Identified volumetric and surface-specific electrochemically active surface area ($ECSA_v$ and $ECSA_a = d_{fa} \cdot a_{cat}$) and apparent thickness L of liquid electrolyte layer between catalyst and gas phase in flooded agglomerate in dependency to the electrode thickness. (D) Local CO_2 concentration and pH as well as (E) local profiles of Faradaic current densities and FE_{CO}, and (F) absolute chemical and electrochemical CO_2 consumption rate and the carbon efficiency CE along flooded agglomerate for 200 μm (solid lines) and 390 μm electrode thickness (dashed lines) at 200 mA cm^{-2}. Measurements were done in a flow cell with 1 M $KHCO_3$, and potentials are iR-corrected.

Table 1
Electrode and operating parameters and the respective identified parameters of electrolyte intrusion and electrochemically active surface area for electrodes with different PTFE content, number of spray-coated layers and pressure differences between gas and electrolyte side: electrode thickness d_{GDE} (determined with a thickness dial gauge by averaging between six measuring points), Ag catalyst loading, porosity ε, thickness of flooded agglomerate d_{fa}, flooding degree, specific surface area of the gas/liquid interface S_{gl}, volumetric surface area of Ag catalyst a_{cat}, electrochemically active surface area ECSA, and apparent thickness of the electrolyte layer between gas and catalyst L.

	d_{GDE}[a] / μm	Catalyst loading[a] / mg_{Ag} cm^{-2}	ε[b] / -	d_{fa}[c] / μm	Flooding degree[d] $\frac{d_{fa}}{d_{GDE}} \cdot 100\%$	S_{gl}[c] / -	a_{cat}[c] / m^2 m^{-3}	$ECSA_v$[d] / m^2 m^{-3}	$ECSA_a$[d] / m^2 m^{-2}	L[d] / μm
1 wt% PTFE; 50 layers; 100 mbar	200 ± 6	70.64	0.4	192.62	96.31 %	57.3	10.5×10^5	10.08×10^5	201.5	3.4
1 wt% PTFE; 80 layers; 100 mbar	275 ± 7	122.03		246.65	89.69 %	50.0	9.09×10^5	8.15×10^5	224.2	5.0
1 wt% PTFE; 110 layers; 100 mbar	390 ± 7	189.64		289.37	74.20 %	60.0	9.04×10^5	6.71×10^5	261.6	4.8
3 wt% PTFE; 80 layers; 20 mbar	391 ± 10	183.41	0.355	247.61	63.17 %	18.8	3.13×10^5	1.98×10^5	77.5	13.2
3 wt% PTFE; 80 layers; 60 mbar	350 ± 5	165.86		277.03	70.67 %	18.3	4.14×10^5	2.92×10^5	114.6	15.1
3 wt% PTFE; 80 layers; 100 mbar	323 ± 10	149.30		317.44	98.28 %	38.4	5.27×10^5	5.18×10^5	167.3	8.3
2 wt% PTFE; 80 layers; 100 mbar	311 ± 7	130.38	0.37	222.96	71.69 %	30.9	9.07×10^5	6.51×10^5	202.4	7.2

[a] measured.
[b] prior work [32].
[c] model parametrization to experiments.
[d] calculated from other parameters.

agglomerate thickness d_{fa} from 248 μm to 317 μm (Table 1). The origin of this strong increase in wetting motivates future studies in this area.

The FE_{CO} is much more sensitive to changes in differential pressure than the electrode potential, as evidenced by only 10 % improvement in potential vs. 25 % improvement in FE_{CO} when increasing pressure from 20 to 100 mbar at 200 mA cm^{-2} (Fig. 6B). At low current densities up to 30 mA cm^{-2}, a high differential pressure of 100 mbar yields the lowest FE_{CO}. Conversely, at higher current densities, the decline in FE_{CO} with increasing current density is less pronounced for the elevated differential pressure. Thus, optimal differential pressure changes with the current density applied.

The simulation replicates the increase of FE_{CO} at high current densities for increasing differential pressure primarily by a larger gas/liquid interface: The interfacial area ratio S_{gl} doubles from 19 to 38 for an

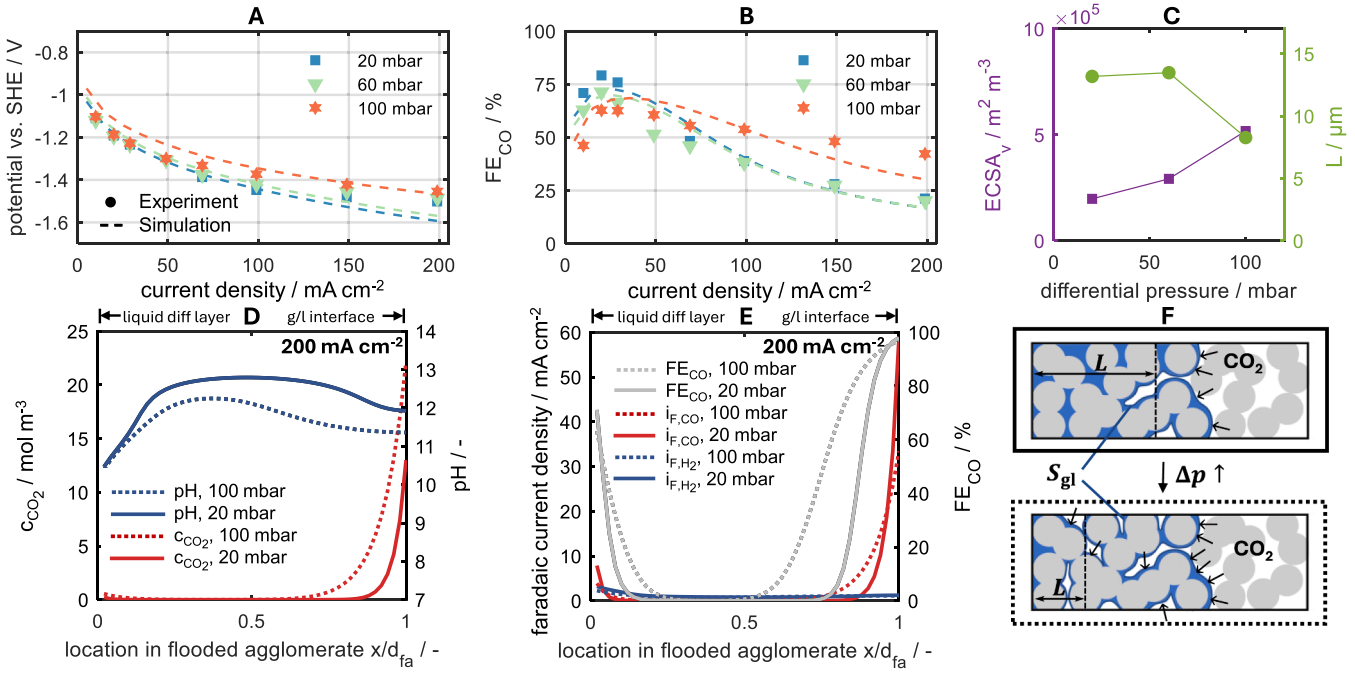

Fig. 6. Impact of differential pressure on GDE performance and state: Experimental and simulated (A) polarization curves and (B) FE_{CO} (electrode layers: 80, i.e. electrode thickness around 350 µm, PTFE content: 3 wt%). (C) Identified volumetric electrochemically active surface area ($ECSA_v$) and apparent thickness L of liquid electrolyte layer between catalyst and gas phase in flooded agglomerate in dependency to the differential pressure. (D) Local CO_2 concentration and pH as well as (E) local profiles of Faradaic current densities and FE_{CO} along flooded agglomerate for 20 mbar (solid line) and 100 mbar differential pressure (dashed line) at 200 mA cm^{-2}. (F) Illustration of the increase in the gas/liquid interface by increasing differential pressure. Measurements were done in a flow cell with 1 M $KHCO_3$, and potentials are iR-corrected.

increase of the differential pressure from 20 to 100 mbar (Table 1). This in turn shortens the apparent thickness of the electrolyte layer between gas and catalyst L by 50 %, reducing it to a value of around 8.28 µm for a differential pressure of 100 mbar (Fig. 6C). Although the thickness of the flooded agglomerate increases, the increase in differential pressure promotes the selective flooding of pores in the electrode, resulting in a more dispersed distribution of electrolyte and thus increasing the size of the gas/liquid interface (Fig. 6F). This effect was also visible in the experiments by the occurrence of electrolyte permeation on the gas-exposed side, even at high applied differential pressures.

The concentration profile of CO_2 along the flooded agglomerate for high current densities shows that higher differential pressures result in a locally higher CO_2 concentration close to the gas/liquid interface (Fig. 6D). This is, on the one hand, due to the larger gas-liquid boundary available for the CO_2 phase transition. On the other hand, a higher differential, and thus higher partial pressure leads, according to Henry's law, to higher solubility of CO_2. The higher CO_2 availability is also reflected in significantly higher values for the FE_{CO} in the local profile (Fig. 6E).

In conclusion, higher differential pressures facilitate CO_2 dissolution on the gas side and create a larger gas/liquid interface. This leads to increased local CO_2 concentration throughout the flooded agglomerate. Enhanced CO_2 availability in turn results in higher FE_{CO} and lower local pH values. Higher pressures indeed have improved the CO_2R-active region of the electrode from 20 % to more than 50 % of the flooded electrode at 200 mA cm^{-2}.

2.5. Influence of PTFE mass fraction

PTFE plays a decisive role in imparting hydrophobic properties to the porous electrode, and thus mitigating the risk of complete pore flooding by the electrolyte. Here, we study the impact of PTFE content on electrolyte intrusion, local electrode states, and on performance. PTFE content was varied between 1 and 3 wt% PTFE mass fractions for 100 mbar overpressure and electrodes of roughly 300 µm.

Experimental and simulation results of polarization and FE_{CO}-current density curves are shown in Fig. 7A and B. The experimental study shows that a lower PTFE content in the electrode correlates with reduced potential losses across the entire current range (Fig. 7A). Reproducing the experiment with the model reveals a significant decrease of up to 36 % in the ECSA with increasing PTFE content (Fig. 7C). A reconstruction of the microstructure from FIB-SEM experiments confirms the ECSA changes as a low fraction of only 62 % of pore walls is not covered by PTFE for an electrode with a high PTFE content of 3 wt% (Table S2). Beyond catalyst surface coverage, excessively high PTFE content hinders catalyst surface wetting, leading to reduced effective electrochemically active surface area (Fig. 7F).

Apart from a higher ECSA, the electrode with a lower PTFE content shows higher FE_{CO} values for current densities above 20 mA cm^{-2} (Fig. 7B). The concentration profile of CO_2 at a current density of 200 mA cm^{-2} exhibits higher dissolved CO_2 concentration for a lower PTFE content (Fig. 7D). This is caused by a decrease in the thickness of the flooded agglomerate d_{fa} for less PTFE from 317 to 289 µm (Table 1), resulting in a lower value of L and in shorter transport distances of dissolved CO_2 as shown in Fig. 7C. The observation that a higher PTFE content leads to increased flooding of the electrode, was also noted by Bienen et al. [46]. They observed an earlier electrolyte breakthrough with higher PTFE content with the same kind of electrodes. Possible reasons for this unintuitive behavior could be increasing capillary forces with decreasing pore size at a higher PTFE amount or a 'slipping' of electrolyte over the less rough PTFE surface [46]. Nevertheless, having at least small amounts of PTFE is essential for GDE operation. Pure Ag GDEs without PTFE experienced strong electrolyte permeation on the gas side and showed an FE_{CO} of 0, even at low current densities (not shown here). This indicates that the electrodes were completely flooded with electrolyte and lost their functionality.

The shorter diffusive transport distances of CO_2 observed with lower PTFE content result in a lower local pH (Fig. 7D) and an increase in local

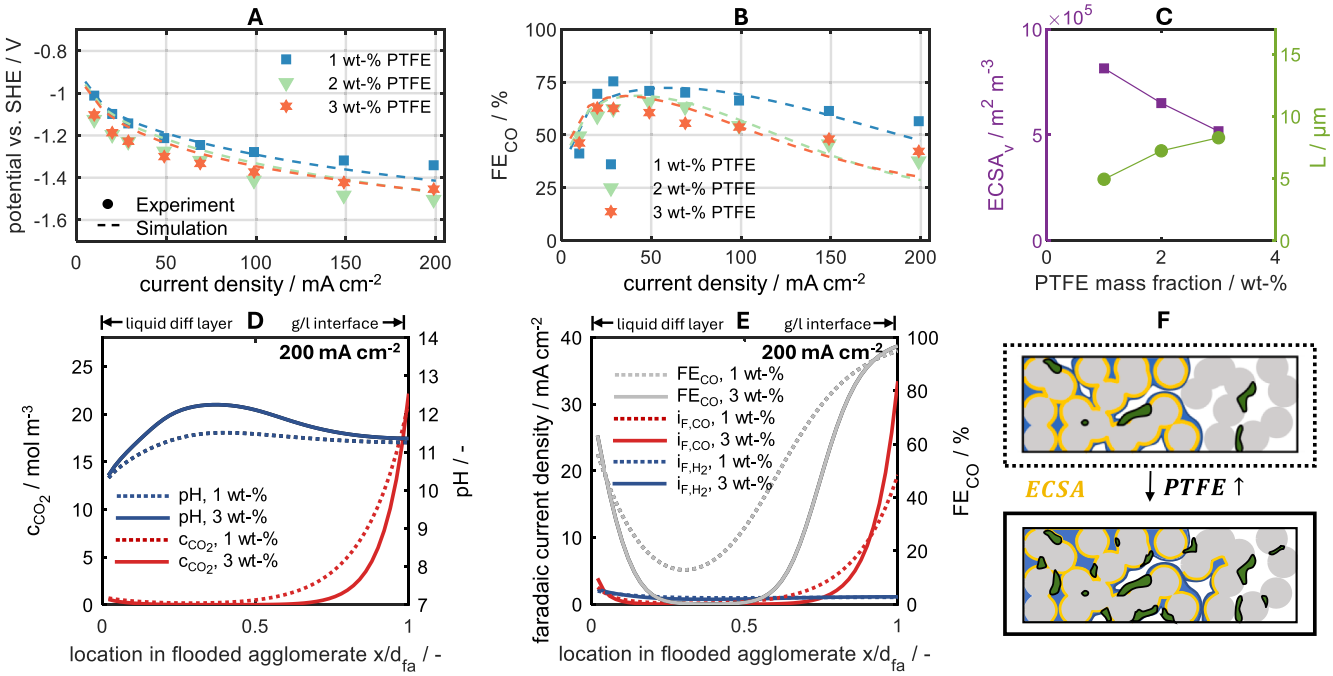

Fig. 7. Impact of PTFE mass fraction on GDE performance and state: Experimental and simulated (A) polarization curves and (B) FE_{CO} (differential pressure: 100 mbar, electrode layers: 80, i.e. electrode thickness around 300 µm). (C) Identified volumetric electrochemically active surface area ($ECSA_v$) and apparent thickness L of liquid electrolyte layer between catalyst and gas phase in flooded agglomerate in dependency to the PTFE fraction. (D) Local CO_2 concentration and pH as well as (E) local profiles of Faradaic current densities and FE_{CO} along flooded agglomerate for 3 wt% (solid line) and 1 wt% differential pressure (dashed line) at 200 mA cm^{-2}. (F) Illustration of increase of PTFE proportion resulting in a decrease in ECSA. Measurements were done in a flow cell with 1 M $KHCO_3$, and potentials are iR-corrected.

FE_{CO} at 200 mA cm^{-2} (Fig. 7E).

Therefore, tuning PTFE content and distribution is essential to stabilize the gas/liquid boundary in the electrode. The goal is to adjust PTFE content such as to establish a stable phase boundary with a good gas supply, and as little PTFE as possible to avoid blocking of catalyst surface resulting in higher potential losses.

Interestingly, electrode performances of the 2 and 3 wt% PTFE electrodes are nearly identical although the values of $ECSA_v$ and apparent electrolyte layer thickness L are different. This is caused by two aspects. Firstly, the higher $ECSA_v$ decreases FE_{CO} whereas the lower diffusion length of CO_2 increases FE_{CO}. Thus, a combination of both results in similar FE_{CO}. Both phenomena do not contribute equally to the change in performance, which is why a further increase in L and a decrease in $ECSA_v$ leads to a change in FE_{CO}, as is the case with the electrode with 1 wt% PTFE.

To show clearly the impact of the single model parameters on electrode performance, a local sensitivity analysis is discussed in the Supporting Information (Section 5). This analysis indicates that performance improvements are primarily achieved by enhancing liquid and gaseous transport, for instance, by decreasing electrode porosity. Increasing ECSA, such as through the use of nanoparticles, carries the risk of exacerbating CO_2 transport limitations, leading to a decrease in FE_{CO}, particularly at high current densities. These findings highlight that, beyond ensuring high CO_2 availability, electrode design and operating parameters must also provide sufficient electrolyte exchange. Besides the measures presented here, this may also be achieved, for example, through high electrolyte flow rates or integrated electrolyte channels within the electrodes. In addition, scaling to larger electrode formats is likely to amplify the impact of these transport phenomena, potentially necessitating the inclusion of three-dimensional effects in future analyses. The evaluation of such approaches warrants further investigation.

3. Conclusions

This study revealed that a high Faradaic efficiency for CO_2 reduction in carbon-free Ag GDEs requires high transport rates of dissolved CO_2 and liquid electrolyte. High CO_2 availability can be achieved by increasing the pressure on the gas side to approx. 100 mbar to increase the gas/liquid interface. A large gas/liquid interface is also enabled by adjusting a low fraction of approx. 1 wt% of PTFE in the GDE. Both insufficient and excessive PTFE contents were found to be disadvantageous, as they promoted flooding and consequently enhanced the HER. Excessive PTFE also led to a reduction in the ECSA. Moreover, thinner electrodes with a shorter transport distance of liquid electrolyte enhance Faradaic efficiency and carbon efficiency for electrochemical CO_2 reduction by better access to fresh electrolyte. These findings help to position carbon-free gas diffusion electrodes as a competitive design for CO_2 reduction. We focused on three influential operation and electrode parameters, as well as current densities $\leq$ 200 mA cm^{-2}, in order to ensure stable operation of the given electrodes and to develop a mechanistic understanding of how these parameters affect electrode performance. Furthermore, the presented method identifies fundamental transport phenomena and design-performance relationships. These are qualitatively transferable across a broad range of GDE architectures, further operation and electrode parameters, the analysis of non-steady states, long-term durability, and higher current densities in future research, enabling a deep understanding of the underlying processes.

4. Experimental section

4.1. Electrode preparation

Carbon-free Ag GDEs were produced according to the procedure described by Franzen et al. [47] by using the wet spraying method developed by Moussallem et al. [47,48]. The procedure for suspension and electrode preparation has been previously published in Osiewacz

et al. [49] but is described here again for clarity and ease of understanding. A mixture of 30 g silver particles (SF9ED, Ames Goldsmith), 50 g 1 wt% hydroxyethyl methyl cellulose (HEMC) solution (Walcocel MKX 70000 PP 01, Wolff Cellulosics), 1.57 g 59 wt% polytetrafluoroethylen (PTFE) dispersion (TF5060GZ, 3 M Dyneon), and 40 g deionized water was prepared. The suspension was stirred with a disperser (Ultra-Turrax T25, IKA) at 13,500 rpm for a total of 10 min with a 5 min break after 5 min. The suspension was then airbrushed onto a nickel mesh (106 μm x 118 μm, 63 μm wire thickness, Haver & Boecker) on a hot plate at 100 °C using a spraying pistol with a 0.6 mm pin hole (Evolution, Harder & Steenbeck). A defined number of layers were sprayed onto each side of the nickel mesh, while pausing until the previous layer was dried before applying a new one. Afterwards, the electrodes were hot pressed (LaboPress P200S, Vogt) at 130 °C and 15 MPa for 5 min and sintered for 15 min at 330 °C [49]. The PTFE content was adjusted to values of 1, 2, and 3 wt% PTFE in the electrode by varying PTFE proportion in suspension recipe. To change the electrode thickness of the GDEs, the total number of coating layers was changed from 80 layers as a standard thickness to values of 50 and 110. The resulting thickness was determined with a thickness dial gauge (FD 50, Käfer GmbH) by averaging between six measuring points. Electrode details can be found in Table 1. A 3D FIB-SEM reconstruction of the porous electrode structure, exemplarily shown for a 97 wt% Ag GDE, is presented in the Supporting Information Section 6. Additional SEM analyses of these electrodes with varying PTFE contents are available in Franzen et al. [47] and are shown in the Supporting Information.

4.2. Electrochemical characterization and product analysis

The GDEs were characterized in a commercial flow cell (Micro Flow Cell V1_2017, ElectroCell) with an active electrode area of 10 cm^2. A new GDE was used for each polarization curve in order to avoid changes due to ageing. A three-electrode setup was used, employing a flat IrO_2 coated electrode as counter electrode and a micro-Ag/AgCl electrode (ET072–1, eDAQ) as reference. Catholyte and anolyte chambers were separated by an anion exchange membrane (fumasep® FAA-3-130-PK, fumatech), and were supplied with 1 M $KHCO_3$ (> 99 wt%, Carl Roth) electrolyte at 960 mL min^{-1}. CO_2 (99.995 %, Linde) was supplied to the gas side of the GDE at a flow rate of 83.58 NmL min^{-1}. Pressure in the electrolyte chambers set to 1000 mbar, while the gas pressure was varied between experiments from 1020 to 1100 mbar. Both pressures were controlled by control circuits, employing needle valves in the gas outlet stream and pressure sensors at the cell inlets. The temperature was not externally controlled. Galvanostatic current was supplied by an electrochemical workstation (ZenniumPro, Zahner) from 10 to 200 mA cm^{-2}; the polarization curves used the cathode potential obtained after keeping a steady current for 40 min at each current density. The cathode potential was measured continuously against the reference electrode, which was placed at the catholyte side of the cell and time-averaged for each current density after being iR-corrected using the high-frequency response (> 10 kHz) [50]. Gas products were sampled from the gas and electrolyte side of the cell and quantified using gas chromatography (Trace1310, ThermoFisher) employing two thermal conductivity detectors (TCD) in a two column setup with a Haysep Q column and a 5 Å mole sieve with a temperature ramp from 50 to 120 °C within 9 min. For FE_{CO}-current density curves, the last GC injection sample of each current step was evaluated. FE_{H2} and total FE are provided in the Supporting Information (Section 7).

5. Model and simulation details

We developed a 1D-model to simulate the reaction and transport processes and states in the electrodes including the electrolyte distribution for different operating conditions and designs of GDEs. The kinetic description for the surface reactions and carbonation, as well as diffusion coefficients and gas/liquid phase transition properties of the

Table 2
Material, design and kinetic parameters which kept constant for all simulations.

Parameter	Symbol	Value	Unit	Source
Operating conditions				
Concentration of electrolyte	c_{elyt}	1	mol L^{-1}	
Pressure of electrolyte side	p_{liq}	1	atm	
Pressure of gas side	p_{tot}	$p_{liq} + \Delta p$	atm	
Temperature	T	298.15	K	
Geometrical surface area of electrode	A_{geom}	10	cm^2	
Internal ohmic resistance	R_{int}	1	Ω	a
Liquid diffusion layer thickness	δ	50×10^{-6}	m	b
Electrochemical surface reaction				
Reaction rate constant of forward reaction for first step of electrochemical CO_2 reduction into CO	$k_{0,f,CO_2R,1}$	5.325×10^{-8}	mol m^{-2} s^{-1}	b
Reaction rate constant of forward reaction for second step of electrochemical CO_2 reduction into CO	$k_{0,f,CO_2R,2}$	2.465×10^{-4}	mol m^{-2} s^{-1}	b
Reaction rate constant of forward reaction for Volmer step of HER	$k_{0,f,HER,1}$	1.497×10^{-8}	mol m^{-2} s^{-1}	b
Reaction rate constant of forward reaction for Heyrovsky step of HER	$k_{0,f,HER,2}$	6.937×10^{-5}	mol m^{-2} s^{-1}	b
Reaction rate constant of backward reaction for first step of electrochemical CO_2 reduction into CO	$k_{0,b,CO_2R,1}$	2.566×10^{-23}	mol m^{-2} s^{-1}	b
Reaction rate constant of backward reaction for second step of electrochemical CO_2 reduction into CO	$k_{0,b,CO_2R,2}$	1.079×10^{-25}	mol m^{-2} s^{-1}	b
Reaction rate constant of backward reaction for Volmer step of HER	$k_{0,b,HER,1}$	6.582×10^{-21}	mol m^{-2} s^{-1}	b
Reaction rate constant of backward reaction for Heyrovsky step of HER	$k_{0,b,HER,2}$	2.776×10^{-25}	mol m^{-2} s^{-1}	b
Charge transfer coefficient for CO_2 reduction	α_{CO_2R}	0.50	–	b
Charge transfer coefficient for hydrogen evolution reaction	α_{HER}	0.76	–	b
Standard redox potential of CO_2R	$E^{00}_{CO_2R}$	− 0.11	V	[54]
Standard redox potential of HER	E^{00}_{HER}	0	V	[54]
Specific capacitance of electrochemical double layer for flat surface	C^{flat}_{DL}	0.5	F m^{-2}	a
Concentration of surface adsorption sites for flat surface	Γ^{flat}	7.04×10^{-6}	mol m^{-2}	[54]
Electrolyte conditions				
Activity coefficient of dissolved species j	γ_j	1	–	assumed
Standard concentration of dissolved species j	c^o_j	1	kmol m^{-3}	
Reaction rate constant for forward reaction of water dissociation	$k_{f,w}$	2.4×10^{-2}	mol m^{-3} s^{-1}	[52]
Equilibrium constant for water dissociation	K_w	1×10^{-8}	mol^2 m^{-6}	[53]
Reaction rate constant of chemical CO_2-to-bicarbonate reaction	$k_{f,c1}$	5.93	m^3 mol^{-1} s^{-1}	[52]

(continued on next page)

Table 2 (*continued*)

Parameter	Symbol	Value	Unit	Source
Equilibrium constant of chemical CO_2-to-bicarbonate reaction	K_{c1}	4.44×10^{4}	$m^3\ mol^{-1}$	[53]
Reaction rate constant of chemical bicarbonate-to-carbonate reaction	$k_{f,c2}$	1×10^{5}	$m^3\ mol^{-1}\ s^{-1}$	[52]
Equilibrium constant for chemical bicarbonate-to-carbonate reaction	K_{c2}	4.66	$m^3\ mol^{-1}$	[53]
Transport parameters				
Binary diffusion coefficient of dissolved CO_2 in water	$D^{liq}_{CO_2,H_2O}$	1.91×10^{-9}	$m^2\ s^{-1}$	[55]
Self diffusion coefficient of liquid H_2O	$D^{liq}_{H_2O}$	2.57×10^{-9}	$m^2\ s^{-1}$	[56]
Binary diffusion coefficient of dissolved CO in water	D^{liq}_{CO,H_2O}	1.99×10^{-9}	$m^2\ s^{-1}$	[57]
Binary diffusion coefficient of liquid H_2 in water	$D^{liq}_{H_2,H_2O}$	2.28×10^{-9}	$m^2\ s^{-1}$	[58]
Binary diffusion coefficient of OH^- in water	D_{OH^-,H_2O}	5.27×10^{-9}	$m^2\ s^{-1}$	[58]
Binary diffusion coefficient of H^+ in water	D_{H^+,H_2O}	9.31×10^{-9}	$m^2\ s^{-1}$	[58]
Binary diffusion coefficient of HCO_3^- in water	$D_{HCO_3^-,H_2O}$	1.19×10^{-9}	$m^2\ s^{-1}$	[58]
Binary diffusion coefficient of CO_3^{2-} in water	$D_{CO_3^{2-},H_2O}$	0.92×10^{-9}	$m^2\ s^{-1}$	[58]
Binary diffusion coefficient of K^+ in water	D_{K^+,H_2O}	1.96×10^{-9}	$m^2\ s^{-1}$	[58]

[a] measured
[b] model parametrization to experiments

electrolyte were taken from the previous model of CO_2R at a silver rotating disc electrode [7]. These were integrated into a GDE model, which was inspired by a GDE model for an cathode involved in oxygen reduction reaction [51].

5.1. Model description

The model and its processes and domains are depicted in Fig. 1.

The GDE is partly flooded by electrolyte. It contains a porous Ag structure that facilitates the reaction and transport of dissolved and gaseous reactants and products. It provides a two-phase boundary between electrolyte and catalyst, which is the ECSA. The at least partially flooded area is called flooded agglomerate (fa) in the following. It is the area where the electrochemical reactions take place. These are the electrochemical CO_2 reduction into CO and hydrogen evolution reaction, which we model using the following lumped microkinetic mechanisms:

$$CO_{2(diss)} + e^- + [\ ] \overset{r_{CO2R.1}}{\rightleftarrows} CO^{\bullet-}_{2(ads)} \tag{8}$$

$$CO^{\bullet-}_{2(ads)} + H_2O + e^- \overset{r_{CO2R.2}}{\rightleftarrows} CO + 2OH^- + [\ ] \tag{9}$$

$$H_2O + e^- + [\ ] \overset{r_{HER.1}}{\rightleftarrows} H^{\bullet}_{(ads)} + OH^- \tag{10}$$

$$H^{\bullet}_{(ads)} + H_2O + e^- \overset{r_{HER.2}}{\rightleftarrows} H_2 \quad + OH^- + [\ ] \tag{11}$$

[] denotes a free surface site. The electrochemical reaction rate r_i of each surface reaction i is calculated by a Butler-Volmer-type kinetic equation (Table 3, Eq. (18)-(21)). The activities of involved species a_j were calculated assuming ideal behavior of diluted solution with the activity coefficients γ_j set to 1 and a standard concentration $c_j^{\ominus}$ of 1 M according to

$$a_j = \gamma_j \frac{c_j}{c_j^{\ominus}}. \tag{12}$$

The activity of water is set to 1 due to the high concentration of it in the electrolyte.

The electrolyte is transported to the GDE through a liquid diffusion layer (ldl) adjacent to the GDL (Table 3, Eq. (32)-(34)). Everywhere in the electrolyte phase, alkaline carbonation reactions are considered according to

$$H_2O \overset{r_w}{\rightleftarrows} H^+ + OH^- \tag{13}$$

$$CO_2 + OH^- \overset{r_{c1}}{\rightleftarrows} HCO_3^- \tag{14}$$

$$HCO_3^- + OH^- \overset{r_{c2}}{\rightleftarrows} CO_3^{2-} + H_2O. \tag{15}$$

Kinetic parameters for these reactions are adapted from seawater analysis and can be found in [52,53]. The reaction rates are calculated using the concentration-dependent power law (Table 3, Eq.(28)-(31)).

On the opposing side of the electrode, CO_2 gas is introduced into the GDE. The gas/liquid interface in the electrode is delineated by a liquid thin film (tf). In this thin film, only species transport takes place (Table 3, Eqs. (39) and (40)). At the gas/liquid interface, phase transition phenomena occur, i.e., dissolution of gaseous CO_2 into the liquid phase described by Henry's law (Table 3, Eq. (45)), evaporation of water into the gas phase described by Raoult's law (Table 3, Eq. (46)), and complete outgassing of dissolved CO and H_2 is assumed at the gas/liquid interface due to low solubility of these gases (Table 3, Eq. (47)). Flooding of single pores leads to an increase in the gas/liquid interface A_{gl} compared to the geometrical area of the electrode A_{geom}, and thus to an increase in gas/liquid phase transition. The increase in area is accounted for in the model by introducing the parameter S_{gl}, the ratio of specific surface area of the interface per geometrical electrode area (details see Röhe et al. [51]):

$$S_{gl} = \frac{A_{gl}}{A_{geom}}. \tag{16}$$

This approach thus corresponds to a homogenization of heterogeneous electrolyte intrusion and in a simple manner allows us to identify changes in the gas/liquid interphase from experiments and assess the effect of electrolyte intrusion behavior on the polarization curve and Faradaic efficiency. As different morphology, composition, and operating conditions lead to different intrusion patterns, this parameter needs to be adjusted for each electrode (for details, see Section 5.2) and operating parameter set individually to reproduce the measurements.

Kinetic and intrusion-specific model parameters are listed in Table 1 and Table 2.

Species transport in the gaseous phase is described by Fickian diffusion and convective Stefan flow (Table 3, Eq. (41)), and in the liquid phase it is described by the Nernst-Planck equation with Fickian diffusion and ion migration (Table 3, Eqs. (32), (35), and (39)). The binary diffusion coefficients were calculated for the gaseous phase with the Chapman-Enskog method (details are shown in SI). In the porous electrode, effective diffusion coefficients of the species are calculated by considering the porosity of the electrode ε and the Bruggemann correlation for tortuosity τ (Table 3, Eqs. (35) and (41)):

$$\tau = \varepsilon^{-0.5}. \tag{17}$$

The mobility of dissolved species is approximated by the Nernst-Einstein equation.

5.2. Numerical simulation and parametrization

The model was implemented in MATLAB R2022b, and differential equations were solved with the ode15s solver. Spatial, one-dimensional

Table 3
Model equations.

Electrochemical reaction kinetics and charge balance		
Reaction rate for first step of electrochemical CO_2 reduction into CO	$r_{\mathrm{CO_2R,1}} = k_{\mathrm{f,CO_2R,1}} \cdot \exp\left(\frac{-(1-\alpha_{\mathrm{CO_2R}})\mathrm{F}}{\mathrm{RT}} \cdot \eta_{\mathrm{CO_2R}}\right) \cdot a_{\mathrm{cat}} \cdot a_{\mathrm{CO_2}} \cdot \theta_0 - k_{\mathrm{b,CO_2R,1}} \cdot \exp\left(\frac{\alpha_{\mathrm{CO_2R}}\mathrm{F}}{\mathrm{RT}} \cdot \eta_{\mathrm{CO_2R}}\right) \cdot a_{\mathrm{cat}} \cdot \theta_{\mathrm{CO_2^{\bullet-}}}$	(18)
Reaction rate for second step of electrochemical CO_2 reduction into CO	$r_{\mathrm{CO_2R,2}} = k_{\mathrm{f,CO_2R,2}} \cdot \exp\left(\frac{-(1-\alpha_{\mathrm{CO_2R}})\mathrm{F}}{\mathrm{RT}} \cdot \eta_{\mathrm{CO_2R}}\right) \cdot a_{\mathrm{cat}} \cdot \theta_{\mathrm{CO_2^{\bullet-}}} - k_{\mathrm{f,CO_2R,2}} \cdot \exp\left(\frac{\alpha_{\mathrm{CO_2R}}\mathrm{F}}{\mathrm{RT}} \cdot \eta_{\mathrm{CO_2R}}\right) \cdot a_{\mathrm{cat}} \cdot \theta_0 \cdot a_{\mathrm{CO}} \cdot a_{\mathrm{OH^-}}^2$	(19)
Reaction rate for Volmer step of HER	$r_{\mathrm{HER,1}} = k_{\mathrm{f,HER,1}} \cdot \exp\left(\frac{-(1-\alpha_{\mathrm{HER}})\mathrm{F}}{\mathrm{RT}} \cdot \eta_{\mathrm{HER}}\right) \cdot a_{\mathrm{cat}} \cdot \theta_0 - k_{\mathrm{b,HER,1}} \cdot \exp\left(\frac{\alpha_{\mathrm{HER}}\mathrm{F}}{\mathrm{RT}} \cdot \eta_{\mathrm{HER}}\right) \cdot a_{\mathrm{cat}} \cdot \theta_{\mathrm{H^\bullet}} \cdot a_{\mathrm{OH^-}}$	(20)
Reaction rate for Heyrovsky step of HER	$r_{\mathrm{HER,2}} = k_{\mathrm{f,HER,2}} \cdot \exp\left(\frac{-(1-\alpha_{\mathrm{HER}})\mathrm{F}}{\mathrm{RT}} \cdot \eta_{\mathrm{HER}}\right) \cdot a_{\mathrm{cat}} \cdot \theta_{\mathrm{H^\bullet}} - k_{\mathrm{b,HER,2}} \cdot \exp\left(\frac{\alpha_{\mathrm{HER}}\mathrm{F}}{\mathrm{RT}} \cdot \eta_{\mathrm{HER}}\right) \cdot a_{\mathrm{cat}} \cdot a_{\mathrm{H_2}} \cdot a_{\mathrm{OH^-}} \cdot \theta_0$	(21)
Charge balance	$\frac{\mathrm{d}E}{\mathrm{d}t} = \frac{1}{C_{\mathrm{DL}}^{\mathrm{flat}} \cdot d_{\mathrm{fa}} \cdot a_{\mathrm{cat}}} (i - \mathrm{F}\sum_i r_i)$	(22)
		(23)
Nernst equation to calculate overpotential for reaction i	$\eta_{\mathrm{i}} = E - (E_i^{00} - 2.303\frac{\mathrm{RT}}{\mathrm{F}} \cdot \mathrm{pH})$	(24)
Faradaic current density	$i_{\mathrm{F,CO}} = \mathrm{F} \cdot (r_{\mathrm{CO_2R,1}} + r_{\mathrm{CO_2R,2}})$	(25)
	$i_{\mathrm{F,H_2}} = \mathrm{F} \cdot (r_{\mathrm{HER,1}} + r_{\mathrm{HER,2}})$	(26)
Faradaic efficiency of carbon monoxide	$FE_{\mathrm{CO}} = \frac{i_{\mathrm{F,CO}}}{i_{\mathrm{F,CO}} + i_{\mathrm{F,H_2}}}$	(27)
Chemical carbonation reaction kinetics		
Reaction rates	$r_{\mathrm{w}} = k_{\mathrm{f,w}} - k_{\mathrm{b,w}} \cdot c_{\mathrm{H^+}} \cdot c_{\mathrm{OH^-}}$	(28)
	$r_{\mathrm{c1}} = k_{\mathrm{f,c1}} \cdot c_{\mathrm{CO_2}} \cdot c_{\mathrm{OH^-}} - k_{\mathrm{b,c1}} \cdot c_{\mathrm{HCO_3^-}}$	(29)
	$r_{\mathrm{c2}} = k_{\mathrm{f,c2}} \cdot c_{\mathrm{HCO_3^-}} \cdot c_{\mathrm{OH^-}} - k_{\mathrm{b,c2}} \cdot c_{\mathrm{CO_3^{2-}}}$	(30)
Equilibrium constant	$K_{\mathrm{i}} = \frac{k_{\mathrm{f},i}}{k_{\mathrm{b},i}}$	(31)
Mass balance, species and charge transport		
Liquid diffusion layer:		
Molar transport flux of species j	$N_j = -D_j^{\mathrm{liq}} \nabla c_j - z_j \frac{D_j^{\mathrm{liq}}}{\mathrm{RT}} \mathrm{F} c_j \nabla \phi$	(32)
Balance of species j with transport and a source by chemical reactions L	$\frac{\partial c_j}{\partial t} = -\nabla N_j + \sum_{i=1}^{\mathrm{L}} \nu_{j,i} r_i$	(33)
Ionic charge transport	$i(x) = \mathrm{F}\sum_j z_j \left(-D_j^{\mathrm{liq}} \nabla c_j - z_j \frac{D_j^{\mathrm{liq}}}{\mathrm{RT}} \mathrm{F} c_j \nabla \phi\right) \mathrm{with} \nabla i = 0$	(34)
Flooded agglomerate:		
Molar transport flux of species j	$N_j = -D_j^{\mathrm{liq}} \varepsilon^{1.5} \nabla c_j S_{\mathrm{int}} - z_j \frac{D_j^{\mathrm{liq}} \varepsilon^{1.5}}{\mathrm{RT}} \mathrm{F} c_j \nabla \phi S_{\mathrm{int}} \quad \mathrm{with}\ S_{\mathrm{int}} = S_{\mathrm{gl}}\ \mathrm{for}\ j \in \{\mathrm{CO_2}, \mathrm{H_2}, \mathrm{CO}\}$	(35)
Balance of species j with transport and sources by electrochemical reactions K and chemical reactions L	$\varepsilon \frac{\partial c_j}{\partial t} = -\nabla N_j + \sum_{i=1}^{K} \frac{\nu_{j,i} r_i}{\Delta x} + \sum_{i=1}^{L} \nu_{j,i} r_i$	(36)
Balance of adsorbed species with $k = \left\{[\,], \mathrm{CO_{2(ads)}^{\bullet-}}, \mathrm{H_{(ads)}^{\bullet}}\right\}$	$\frac{\partial \theta_k}{\partial t} = \frac{1}{\Gamma^{\mathrm{flat}} \cdot a_{\mathrm{cat}}} \sum_i \frac{\nu_{k,i} r_i}{\Delta x}$	(37)
Ionic charge transport	$i(x) = \mathrm{F}\sum_j z_j \left(-D_j^{\mathrm{liq}} \varepsilon^{1.5} \nabla c_j - z_j \frac{D_j^{\mathrm{liq}} \varepsilon^{1.5}}{\mathrm{RT}} \mathrm{F} c_j \nabla \phi\right)$	(38)
Liquid thin-film:		
Molar transport flux of species j	$N_j = -D_j^{\mathrm{liq}} \nabla c_j S_{\mathrm{gl}}$	(39)
Balance of species j	$\frac{\partial c_j}{\partial t} = -\nabla N_j$	(40)
Gas phase:		
Molar transport flux of species j	$N_j = -D_{j,\mathrm{CO_2}}^{\mathrm{gas}} \varepsilon^{1.5} \nabla \frac{p_j}{\mathrm{RT}} + \frac{p_j}{\mathrm{RT}} v_{\mathrm{gas}}$	(41)
Balance of species j	$\frac{\varepsilon}{\mathrm{RT}} \frac{\partial p_j}{\partial t} = -\nabla N_j$	(42)
Sum of molar flow due to phase transition processes from liquid to gas or vice versa	$\sum_j N_j^{\mathrm{gl}} = N_{\mathrm{H_2O}}^{\mathrm{evap}} + \mathrm{N}_{\mathrm{CO}}^{\mathrm{gl}} + \mathrm{N}_{\mathrm{H_2}}^{\mathrm{gl}} - \mathrm{N}_{\mathrm{CO_2}}^{\mathrm{sol}}$	(43)
Convective velocity of liquid phase (Stefan flow)	$v_{\mathrm{gas}} = \frac{\sum_j N_j^{\mathrm{gl}} \mathrm{RT}}{p_{\mathrm{tot}}} \mathrm{with} \frac{\mathrm{d}v_{\mathrm{gas}}}{\mathrm{d}x} = 0$	(44)
Phase transition		
Gas/liquid equilibrium CO_2 (Henry's law)	$p_{\mathrm{CO_2}}^* = H_{\mathrm{CO_2}} \cdot c_{\mathrm{CO_2}}^*$	(45)
Gas/liquid equilibrium H_2O (Raoult's law)	$p_{\mathrm{H_2O}}^* = x_{\mathrm{H_2O}} \cdot p_{\mathrm{H_2O}}^0$	(46)
Ideal gas law with $j = \{\mathrm{H_2}; \mathrm{CO}\}$	$p_j^* = c_j^* \mathrm{RT}$	(47)
Boundary conditions		
$KHCO_3$ in electrolyte bulk	$c_{\mathrm{KHCO_3}}(x = -\delta, t) = c_{\mathrm{KHCO_3,bulk}} = \mathrm{const.}$	(48)
CO_2 in gas phase bulk	$p_{\mathrm{CO_2}}(x = x_{\mathrm{gas}}, t) = p_{\mathrm{tot}} = \mathrm{const.}$	(49)
Partial pressure of species i in gas bulk with $j = \{\mathrm{CO_2}; \mathrm{H_2}; \mathrm{H_2O}\}$	$p_j(x = x_{\mathrm{gas}}, t) = 0 = \mathrm{const.}$	(50)
Correction of internal resistance	$E = E_{\mathrm{ext}} - i_{\mathrm{ext}} A_{\mathrm{geom}} R_{\mathrm{int}}$	(51)

discretization from liquid to gas phase (coordinate x in Fig. 1) was done with an equidistant grid with a grid size of $\Delta x = 1$ µm. Lower grid sizes do not lead to a visual change of simulated polarization and Faradaic efficiency-current density curves. For spatial discretization, the finite volume method with central differential quotient was implemented. Boundary conditions for the simulations can be found in Table 3, Eqs. (48)-(50).

For parameter identification, the MATLAB-implemented optimizer patternsearch was used. The kinetic parameters of CO_2R and HER including reaction rate constants of forward and backward reactions and charge transfer coefficients α_{CO_2R} and α_{HER} were identified by using the polarization curve and FE_{CO}-current density curve for the reference case 98 wt% Ag, 80 layers, and 100 mbar. Additionally, the thickness of the liquid diffusion layer δ was identified in this optimization step. These parameters were held constant for all simulative electrode and operating parameter variations.

For identifying flooding state and electrode parameters for the different operating conditions and designs, the thickness of the flooded agglomerate d_{fa}, the specific surface area of the gas/liquid interface S_{gl}, and the intrinsic, volume specific catalyst surface of the electrode a_{cat} were identified by reproducing the polarization curve and Faradaic efficiency-current density curve of the individual measurements by simulation. Identified parameters can be found in Table 1, further model, design, and operating parameters, which were kept constant for all simulations, can be found in Table 2.

CRediT authorship contribution statement

Thomas Turek: Writing – review & editing, Supervision, Project administration, Methodology, Funding acquisition, Formal analysis. **Inga Dorner:** Writing – original draft, Validation, Methodology, Investigation, Formal analysis, Data curation, Conceptualization. **Ulrike Krewer:** Writing – review & editing, Supervision, Project administration, Methodology, Funding acquisition, Formal analysis, Conceptualization. **Maximilian Röhe:** Methodology, Investigation. **Barbara Ellendorff:** Resources, Data curation. **Philipp Röse:** Writing – review & editing, Data curation, Conceptualization. **Jens Osiewacz:** Writing – review & editing, Investigation, Formal analysis, Data curation.

Declaration of Competing Interest

The authors declare that they have no known competing financial interests or personal relationships that could have appeared to influence the work reported in this paper. Reports a relationship with that includes:. Has patent pending to. If there are other authors, they declare that they have no known competing financial interests or personal relationships that could have appeared to influence the work reported in this paper.

Acknowledgments

We are thankful to the German Research Foundation for funding this research in the framework of Research Unit 2397 (KR 3850-6-2 and TU 89-13-2). We would also like to thank Thorben Mager and Ulrich Nieken from the University of Stuttgart for providing the SEM images and image analysis. We acknowledge support by the KITPublication Fund of the Karlsruhe Institute of Technology, Germany.

Appendix A. Supporting information

Supplementary data associated with this article can be found in the online version at doi:10.1016/j.jcou.2025.103163.

Data Availability

The data presented in the manuscript are openly available in the KITopen repository at DOI: https://doi.org/ 10.35097/cwj94nkvmqp3zzp9 [59].

References

[1] S. Nitopi, E. Bertheussen, S.B. Scott, X. Liu, A.K. Engstfeld, S. Horch, B. Seger, I.E. L. Stephens, K. Chan, C. Hahn, J.K. Norskov, T.F. Jaramillo, I. Chorkendorff, Progress and perspectives of electrochemical CO_2 reduction on copper in aqueous electrolyte, Chem. Rev. 119 (2019) 7610–7672, https://doi.org/10.1021/acs.chemrev.8b00705.

[2] A. Bagger, W. Ju, A.S. Varela, P. Strasser, J. Rossmeisl, Electrochemical CO_2 reduction: a classification problem, ChemPhysChem 18 (2017) 3266–3273, https://doi.org/10.1002/cphc.201700736.

[3] M. Jouny, W. Luc, F. Jiao, General techno-economic analysis of CO_2 electrolysis systems, Ind. Eng. Chem. Res. 57 (2018) 2165–2177, https://doi.org/10.1021/acs.iecr.7b03514.

[4] R. Krause, D. Reinisch, C. Reller, H. Eckert, D. Hartmann, D. Taroata, K. Wiesner-Fleischer, A. Bulan, A. Lueken, G. Schmid, Industrial application aspects of the electrochemical reduction of CO_2 to CO in aqueous electrolyte, Chem. Ing. Tech. 92 (2020) 53–61, https://doi.org/10.1002/cite.201900092.

[5] A. Goyal, G. Marcandalli, V.A. Mints, M.T.M. Koper, Competition between CO_2 reduction and hydrogen evolution on a gold electrode under well-defined mass transport conditions, J. Am. Chem. Soc. 142 (2020) 4154–4161, https://doi.org/10.1021/jacs.9b10061.

[6] J. Jang, M. Rüscher, M. Winzely, C.G. Morales-Guio, Gastight rotating cylinder electrode: Toward decoupling mass transport and intrinsic kinetics in electrocatalysis, AIChE J. 68 (2022) e17605, https://doi.org/10.1002/aic.17605.

[7] I. Dorner, P. Röse, U. Krewer, Dynamic vs. stationary analysis of electrochemical carbon dioxide reduction: Profound differences in local states, ChemElectroChem 10 (2023) e202300387, https://doi.org/10.1002/celc.202300387.

[8] N. Gupta, M. Gattrell, B. MacDougall, Calculation for the cathode surface concentrations in the electrochemical reduction of CO_2 in $KHCO_3$ solutions, J. Appl. Electrochem 36 (2006) 161–172, https://doi.org/10.1007/s10800-005-9058-y.

[9] M. Dunwell, X. Yang, B.P. Setzler, J. Anibal, Y. Yan, B. Xu, Examination of near-electrode concentration gradients and kinetic impacts on the electrochemical reduction of CO_2 using surface-enhanced infrared spectroscopy, ACS Catal. 8 (2018) 3999–4008, https://doi.org/10.1021/acscatal.8b01032.

[10] A. Hecimovic, M.T. Mayer, L.G.J. de Haart, S. Gupta, C.K. Kiefer, A. Navarrete, A. Schulz, U. Fantz, Benchmarking microwave-induced CO_2 plasma splitting against electrochemical CO_2 reduction for a comparison of promising technologies, J. CO_2 Util. 83 (2024), https://doi.org/10.1016/j.jcou.2024.102825.

[11] S. Verma, B. Kim, H.R. Jhong, S. Ma, P.J. Kenis, A. Gross-Margin, model for defining technoeconomic benchmarks in the electroreduction of CO_2, ChemSusChem 9 (2016) 1972–1979, https://doi.org/10.1002/cssc.201600394.

[12] B.J.M. Etzold, U. Krewer, S. Thiele, A. Dreizler, E. Klemm, T. Turek, Understanding the activity transport nexus in water and CO_2 electrolysis: state of the art, challenges and perspectives, Chem. Eng. J. 424 (2021) 130501, https://doi.org/10.1016/j.cej.2021.130501.

[13] M. Löffelholz, J. Osiewacz, A. Lüken, K. Perrey, A. Bulan, T. Turek, Modeling electrochemical CO_2 reduction at silver gas diffusion electrodes using a TFFA approach, Chem. Eng. J. 435 (2022) 134920, https://doi.org/10.1016/j.cej.2022.134920.

[14] A.A. Samu, I. Szenti, A. Kukovecz, B. Endrodi, C. Janaky, Systematic screening of gas diffusion layers for high performance CO_2 electrolysis, Commun. Chem. 6 (2023), https://doi.org/10.1038/s42004-023-00836-2.

[15] C. Ampelli, F. Tavella, D. Giusi, A.M. Ronsisvalle, S. Perathoner, G. Centi, Electrode and cell design for CO_2 reduction: a viewpoint, Catal. Today 421 (2023) 114217, https://doi.org/10.1016/j.cattod.2023.114217.

[16] Y. Wu, S. Garg, M. Li, M.N. Idros, Z. Li, R. Lin, J. Chen, G. Wang, T.E. Rufford, Effects of microporous layer on electrolyte flooding in gas diffusion electrodes and selectivity of CO_2 electrolysis to CO, J. Power Sources 522 (2022) 230998, https://doi.org/10.1016/j.jpowsour.2022.230998.

[17] Y. Kong, H. Hu, M. Liu, Y. Hou, V. Kolivoška, S. Vesztergom, P. Broekmann, Visualisation and quantification of flooding phenomena in gas diffusion electrodes used for electrochemical CO_2 reduction: a combined EDX/ICP–MS approach, J. Catal. 408 (2022) 1–8, https://doi.org/10.1016/j.jcat.2022.02.014.

[18] M.E. Leonard, L.E. Clarke, A. Forner-Cuenca, S.M. Brown, F.R. Brushett, Investigating electrode flooding in a flowing electrolyte, gas-fed carbon dioxide electrolyzer, ChemSusChem 13 (2020) 400–411, https://doi.org/10.1002/cssc.201902547.

[19] Y. Wu, L. Charlesworth, I. Maglaya, M.N. Idros, M. Li, T. Burdyny, G. Wang, T. E. Rufford, Mitigating electrolyte flooding for electrochemical CO_2 reduction via infiltration of hydrophobic particles in a gas diffusion layer, ACS Energy Lett. 7 (2022) 2884–2892, https://doi.org/10.1021/acsenergylett.2c01555.

[20] M. Heßelmann, B.C. Bräsel, R.G. Keller, M. Wessling, Simulation-based guidance for improving CO_2 reduction on silver gas diffusion electrodes, Electrochem. Sci. Adv. 3 (2022) 2100160, https://doi.org/10.1002/elsa.202100160.

[21] K. Yang, R. Kas, W.A. Smith, T. Burdyny, Role of the carbon-based gas diffusion layer on flooding in a gas diffusion electrode cell for electrochemical CO_2 reduction, ACS Energy Lett. 6 (2020) 33–40, https://doi.org/10.1021/acsenergylett.0c02184.

[22] H. Rabiee, B. Ma, Y. Yang, F. Li, P. Yan, Y. Wu, X. Zhang, S. Hu, H. Wang, L. Ge, Z. Zhu, Advances and challenges of carbon-free gas-diffusion electrodes (GDEs) for

electrochemical CO_2 reduction, Adv. Funct. Mater. 35 (2025) 2411195, https://doi.org/10.1002/adfm.202411195.
[23] A.H.M. da Silva, S.J. Raaijman, P.J. Corbett, Mesh GDEs: an alternative to carbon-based electrodes for CO_2 reduction at higher current densities, Chem. Eng. J. 494 (2024) 153266, https://doi.org/10.1016/j.cej.2024.153266.
[24] J. Zhang, W. Luo, A. Züttel, Self-supported copper-based gas diffusion electrodes for CO_2 electrochemical reduction, J. Mater. Chem. 7 (2019) 26285–26292, https://doi.org/10.1039/c9ta06736a.
[25] M. Filippi, T. Möller, R. Pastusiak, E. Magori, B. Paul, P. Strasser, Scale-up of PTFE-based gas diffusion electrodes using an electrolyte-integrated polymer-coated current collector approach, ACS Energy Lett. 9 (2024) 1361–1368, https://doi.org/10.1021/acsenergylett.4c00114.
[26] G.O. Larrazabal, P. Strom-Hansen, J.P. Heli, K. Zeiter, K.T. Therkildsen, I. Chorkendorff, B. Seger, Analysis of mass flows and membrane cross-over in CO_2 reduction at high current densities in an MEA-type electrolyzer, ACS Appl. Mater. Interfaces 11 (2019) 41281–41288, https://doi.org/10.1021/acsami.9b13081.
[27] I. Moussallem, J. Jörissen, U. Kunz, S. Pinnow, T. Turek, Chlor-alkali electrolysis with oxygen depolarized cathodes: history, present status and future prospects, J. Appl. Electrochem 38 (2008) 1177–1194, https://doi.org/10.1007/s10800-008-9556-9.
[28] N. Furuya, H. Aikawa, Comparative study of oxygen cathodes loaded with Ag and Pt catalysts in chlor-alkali membrane cells, Electrochim. Acta 45 (2000) 4251–4256, https://doi.org/10.1016/S0013-4686(00)00557-0.
[29] T. Haas, R. Krause, R. Weber, M. Demler, G. Schmid, Technical photosynthesis involving CO_2 electrolysis and fermentation, Nat. Catal. 1 (2018) 32–39, https://doi.org/10.1038/s41929-017-0005-1.
[30] P. Jeanty, C. Scherer, E. Magori, K. Wiesner-Fleischer, O. Hinrichsen, M. Fleischer, Upscaling and continuous operation of electrochemical CO_2 to CO conversion in aqueous solutions on silver gas diffusion electrodes, J. CO_2 Util. 24 (2018) 454–462, https://doi.org/10.1016/j.jcou.2018.01.011.
[31] M. Röhe, A. Botz, D. Franzen, F. Kubannek, B. Ellendorff, D. Öhl, W. Schuhmann, T. Turek, U. Krewer, The key role of water activity for the operating behavior and dynamics of oxygen depolarized cathodes, ChemElectroChem 6 (2019) 5671–5681, https://doi.org/10.1002/celc.201901224.
[32] M. Röhe, D. Franzen, F. Kubannek, B. Ellendorff, T. Turek, U. Krewer, Revealing the degree and impact of inhomogeneous electrolyte distributions on silver based gas diffusion electrodes, Electrochim. Acta 389 (2021) 138693, https://doi.org/10.1016/j.electacta.2021.138693.
[33] M.C. Paulisch, M. Gebhard, D. Franzen, A. Hilger, M. Osenberg, N. Kardjilov, B. Ellendorff, T. Turek, C. Roth, I. Manke, Operando laboratory X-Ray imaging of silver-based gas diffusion electrodes during oxygen reduction reaction in highly alkaline media, Materials 12 (2019) 2686, https://doi.org/10.3390/ma12172686.
[34] H. Hoffmann, M.C. Paulisch, M. Gebhard, J. Osiewacz, M. Kutter, A. Hilger, T. Arlt, N. Kardjilov, B. Ellendorff, F. Beckmann, H. Markötter, M. Luik, T. Turek, I. Manke, C. Roth, Development of a modular operando cell for X-ray imaging of strongly absorbing silver-based gas diffusion electrodes, J. Electrochem. Soc. 169 (2022) 044508, https://doi.org/10.1149/1945-7111/ac6220.
[35] J. Osiewacz, M. Löffelholz, B. Ellendorff, T. Turek, Modeling mass transfer limitations driven by electrowetting in electrochemical CO_2 reduction at silver gas diffusion electrodes, J. Power Sources 603 (2024) 234430, https://doi.org/10.1016/j.jpowsour.2024.234430.
[36] L.M. Baumgartner, A. Goryachev, C.I. Koopman, D. Franzen, B. Ellendorff, T. Turek, D.A. Vermaas, Electrowetting limits electrochemical CO_2 reduction in carbon-free gas diffusion electrodes, Energy Adv. 2 (2023) 1893–1904, https://doi.org/10.1039/d3ya00285c.
[37] L.M. Baumgartner, C.I. Koopman, A. Forner-Cuenca, D.A. Vermaas, When Flooding Is Not Catastrophic—Woven Gas Diffusion Electrodes Enable Stable CO_2 Electrolysis, ACS Appl. Energy Mater. (2022), https://doi.org/10.1021/acsaem.2c02783.
[38] J. Osiewacz, M. Löffelholz, B. Ellendorff, T. Turek, Modeling mass transfer limitations driven by electrowetting in electrochemical CO_2 reduction at silver gas diffusion electrodes, J. Power Sources 603 (2024), https://doi.org/10.1016/j.jpowsour.2024.234430.
[39] D. Franzen, B. Ellendorff, M.C. Paulisch, A. Hilger, M. Osenberg, I. Manke, T. Turek, Influence of binder content in silver-based gas diffusion electrodes on pore system and electrochemical performance, J. Appl. Electrochem 49 (2019) 705–713, https://doi.org/10.1007/s10800-019-01311-4.
[40] T. Hatsukade, K.P. Kuhl, E.R. Cave, D.N. Abram, T.F. Jaramillo, Insights into the electrocatalytic reduction of CO_2 on metallic silver surfaces, Phys. Chem. Chem. Phys. 16 (2014) 13814–13819, https://doi.org/10.1039/c4cp00692e.
[41] E.L. Clark, A.T. Bell, Direct observation of the local reaction environment during the electrochemical reduction of CO_2, J. Am. Chem. Soc. 140 (2018) 7012–7020, https://doi.org/10.1021/jacs.8b04058.
[42] N.T. Nesbitt, T. Burdyny, H. Simonson, D. Salvatore, D. Bohra, R. Kas, W.A. Smith, Liquid–solid boundaries dominate activity of CO_2 reduction on gas-diffusion electrodes, ACS Catal. 10 (2020) 14093–14106, https://doi.org/10.1021/acscatal.0c03319.
[43] M. Neumann, M. Osenberg, A. Hilger, D. Franzen, T. Turek, I. Manke, V. Schimdt, On a pluri-Gaussian model for three-phase microstructures, with applications to 3D image data of gas-diffusion electrodes, Comput. Mater. Sci. 156 (2019) 325–331, https://doi.org/10.1016/j.commatsci.2018.09.033.
[44] B. De Mot, J. Hereijgers, M. Duarte, T. Breugelmans, Influence of flow and pressure distribution inside a gas diffusion electrode on the performance of a flow-by CO_2 electrolyzer, Chem. Eng. J. 378 (2019) 122224, https://doi.org/10.1016/j.cej.2019.122224.
[45] L.M. Baumgartner, C.I. Koopman, A. Forner-Cuenca, D.A. Vermaas, When flooding Is not catastrophic-woven gas diffusion electrodes enable stable CO_2 electrolysis, ACS Appl. Energy Mater. 5 (2022) 15125–15135, https://doi.org/10.1021/acsaem.2c02783.
[46] F. Bienen, M.C. Paulisch, T. Mager, J. Osiewacz, M. Nazari, M. Osenberg, B. Ellendorff, T. Turek, U. Nieken, I. Manke, K.A. Friedrich, Investigating the electrowetting of silver-based gas-diffusion electrodes during oxygen reduction reaction with electrochemical and optical methods, Electrochem. Sci. Adv. 3 (2022) e2100158, https://doi.org/10.1002/elsa.202100158.
[47] D. Franzen, B. Ellendorff, M.C. Paulisch, A. Hilger, M. Osenberg, I. Manke, T. Turek, Influence of binder content in silver-based gas diffusion electrodes on pore system and electrochemical performance, J. Appl. Electrochem 49 (2019) 705–713, https://doi.org/10.1007/s10800-019-01311-4.
[48] I. Moussallem, S. Pinnow, N. Wagner, T. Turek, Development of high-performance silver-based gas-diffusion electrodes for chlor-alkali electrolysis with oxygen depolarized cathodes, Chem. Eng. Process 52 (2012) 125–131, https://doi.org/10.1016/j.cep.2011.11.003.
[49] J. Osiewacz, B. Ellendorff, U. Kunz, T. Turek, Method - Best practices and common pitfalls in experimental investigation of electrochemical CO_2 reduction at gas diffusion electrodes, J. Electrochem. Soc. 171 (2024) 103503, https://doi.org/10.1149/1945-7111/ad7f91.
[50] W. Zheng, iR compensation for electrocatalysis studies: Considerations and recommendations, ACS Energy Lett. 8 (2023) 1952–1958, https://doi.org/10.1021/acsenergylett.3c00366.
[51] M. Röhe, F. Kubannek, U. Krewer, Processes and their limitations in oxygen depolarized cathodes: A dynamic model-based analysis, ChemSusChem 12 (2019) 2373–2384, https://doi.org/10.1002/cssc.201900312.
[52] K.G. Schulz, U. Riebesell, B. Rost, S. Thoms, R.E. Zeebe, Determination of the rate constants for the carbon dioxide to bicarbonate inter-conversion in pH-buffered seawater systems, Mar. Chem. 100 (2006) 53–65, https://doi.org/10.1016/j.marchem.2005.11.001.
[53] R.N. Roy, L.N. Roy, K.M. Vogel, C. Porter-Moore, T. Pearson, C.E. Good, F. J. Millero, D.M. Campbell, The dissociation constants of carbonic acid in seawater at salinities 5 to 45 and temperatures 0 to 45°C, Mar. Chem. 44 (1993) 249–267, https://doi.org/10.1016/0304-4203(93)90207-5.
[54] M.R. Singh, J.D. Goodpaster, A.Z. Weber, M. Head-Gordon, A.T. Bell, Mechanistic insights into electrochemical reduction of CO_2 over Ag using density functional theory and transport models, Proc. Natl. Acad. Sci. 114 (2017) E8812–E8821, https://doi.org/10.1073/pnas.1713164114.
[55] B. Jähne, G. Heinz, W. Dietrich, Measurement of the diffusion coefficients of sparingly soluble gases in water, J. Geophys. Res. 92 (1987) 10.767–10.776, https://doi.org/10.1029/JC092iC10p10767.
[56] J.H. Wang, Self-diffusion coefficients of water, –4412, J. Phys. Chem. C. 69 (1965) 4412, https://doi.org/10.1021/j100782a510.
[57] B.E. Poling, J.M. Prausnitz, J.P. O'Connell, The Properties of Gases And Liquids, fifth edition, McGRAW-HILL, 2004.
[58] M. Flury, T.F. Gimmi, 6.2 Solute Diffusion, in: Methods of Soil Analysis: Part 4 Physical Methods, John Wiley & Sons, 2002, pp. 1323–1351.
[59] I. Dorner, J. Osiewacz, P. Röse, B. Ellendorff, T. Turek, U. Krewer, Research data of publication "Control of electrolyte intrusion in carbon-free silver gas diffusion electrodes for electrochemical CO_2 reduction" [dataset], (2025). https://doi.org/10.35097/cwj94nkvmqp3zzp9.